Magnetic-field dependence of the exciton energy in a quantum disk

K. L. Janssens, F. M. Peeters* and V. A. Schweigert†

Departement Natuurkunde, Universiteit Antwerpen (UIA), Universiteitsplein 1, B-2610 Antwerpen, Belgium
(Received 25 February 2000; revised manuscript received 18 September 2000; published 24 April 2001)

The ground-state energy and binding energy of an exciton, confined in a quantum disk, are calculated as a function of an external magnetic field. The confinement potential is a hard wall of finite height. The diamagnetic shift is investigated for magnetic fields up to 40 T. Our results are applied to $In_yAl_{1-y}As/Al_xGa_{1-x}As$ self-assembled quantum dots, and good agreement with experiments is obtained if we assume that the light hole is involved in the exciton formation. Furthermore, we investigated the influence of the dot size on the diamagnetic shift by changing the disk radius. The exciton excited states are found as a function of the magnetic field. The relative angular momentum is not a good quantum number and its value changes with the magnetic field strength.

I. INTRODUCTION

Recently, there has been much interest in the study of quantum dots, which are structures in which the charge carriers are confined in all three dimensions. Especially the self-assembled quantum dots[1] are considered to be very promising for possible applications, such as quantum dot lasers,[2] due to their large confinement energy and high optical quality. The dots are formed by the Stranski-Krastanow growth mode in which a material, e.g., $In_yAl_{1-y}As$, is deposited on another material with a substantially different lattice parameter, e.g., $Al_xGa_{1-x}As$.[3] The lattice mismatch, which is required for this growth process, is typically about 4%.[4] Initially, the growth is two dimensional (2D), but after a critical thickness of a few monolayers, coherent islands are formed due to strain effects. The shape of the formed islands is not well known, but is expected to resemble a lens or a pyramid. The density, size, and shape of the dots are strongly dependent on the growth conditions. Typical sizes of dots vary between the basis size of 7 and 20 nm and a height of a few nanometers. The density of the dots is of the order 10^{11} cm^{-2}.[2]

The properties of confined excitons have been the subject of many theoretical studies. Bryant[5] used variational and configuration-interaction representations to study excitons in quantum boxes. Later, matrix diagonalization techniques were used to study the exciton energy in a quantum dot with parabolic confinement potential. Song and Ulloa[6] studied the effect of noncircular symmetric structures, and Halonen et al.[7] studied the influence of a magnetic field. More recently, Pereyra and Ulloa[8] investigated magnetic-field and quantum confinement asymmetry effects on excitons, again for the case of parabolic confinement. These studies have shown a strong competition between the quantum dot size, Coulomb interaction, and magnetic confinement.

In the present work, we model the quantum dots by a quantum disk with a hard-wall confinement of finite height[9] and include the mass mismatch between the dot and barrier material. In experimentally realized samples of self-assembled dots one has typically a variation of sizes between the dots of a few percent, and a gradient in the alloy content was found recently,[10] as well as variations in the shape of the dots. Therefore, we believe that our quantum disk model is a reasonable first-order approximation to such self-assembled dots. Here we present a theoretical study of the effect of an external magnetic field on the properties of an exciton in the quantum disk, fully taking into account the Coulomb interaction between the electron and the hole. The ground-state energy and binding energy of the exciton are studied as a function of the magnetic field. This allows us to determine the diamagnetic shift of the exciton, which we find in very good agreement with the experimentally observed shift by Wang et al.[11] In most of the previous theoretical work, this diamagnetic shift was only determined for very low values of the magnetic field, where the confinement energy is larger than the cyclotron energy, and could be approximated by $e^2\langle\rho^2\rangle B^2/8\mu$.[11–13] In our calculations, we consider magnetic fields up to 40 T. For such large magnetic fields, the weak-field approximation is no longer valid, because now the cyclotron energy overcomes the confinement energy and the particles will act rather as free particles in a magnetic field.[14] We find that the magnetic field dependence of the diamagnetic shift can be very closely approximated by $\beta B^2/(1+\alpha B)$. To be able to make a valid comparison between theory and experiment, we considered for our simulations $In_{0.55}Al_{0.45}As$ quantum dots, which were experimentally studied by Wang et al.[11]

The paper is organized as follows. In Sec. II, we present the theoretical model and explain our method of solution. The results for the exciton ground state and the comparison with the experimental results of Ref. 11 are presented in Sec. III. In Sec. IV, we describe the effect of changing the disk radius on the exciton energy and diamagnetic shift. The results for the exciton energy spectrum are presented in Sec. V. Our results are summarized in Sec. VI.

II. THEORETICAL MODEL

The Hamiltonian describing our system is given by

$$H = \sum_{j=1}^{2} H_j(\mathbf{r}_j) + V_c(\mathbf{r}_1 - \mathbf{r}_2), \qquad (1)$$

with

$$H_j = \left(\mathbf{p}_j - \frac{q_j}{c}\mathbf{A}_j\right)\frac{1}{2m_j(\mathbf{r})}\left(\mathbf{p}_j - \frac{q_j}{c}\mathbf{A}_j\right) + V_j(\mathbf{r}_j), \quad (2)$$

where the indices $j=1,2$ correspond to the electron and the hole with masses m_1, m_2, respectively, $V_j(\rho_j, z_j) = 0$ ($\rho_j < R, |z_j| < d/2$), $V_{j,o}$ (otherwise) is the confinement potential with R the radius of the quantum disk and d its thickness, $\rho_j = \sqrt{x_j^2 + y_j^2}$, $V_c(\mathbf{r}) = -e^2/\epsilon|\mathbf{r}|$, and $q_j = \mp e$. Here and below the upper and lower sign correspond to electron and hole, respectively. For convenience we will sometimes also use the notations e, h instead of 1,2. We allow for a difference in mass between the dot region and the region outside the dot: $m_j(\mathbf{r}) = m_{w,j}$ inside the disk and $m_j(\mathbf{r}) = m_{b,j}$ outside the disk. In our numerical work, we used the following values for the physical parameters: $\epsilon = 12.71$, $m_{w,e} = 0.076 m_0$, $m_{b,e} = 0.097 m_0$, $m_{w,h} = m_{b,h} = 0.45 m_0$, $V_{e,o} = 258$ meV, and $V_{h,o} = 172$ meV, which are typical for the In$_{0.55}$Al$_{0.45}$As/Al$_{0.35}$Ga$_{0.65}$As system.

Using cylindrical coordinates $\mathbf{r}_j = (z_j, \rho_j, \phi_j)$ the one-particle Hamiltonian takes the form

$$H_j = -\frac{\hbar^2}{2}\left(\frac{\partial}{\partial z_j}\frac{1}{m_j}\frac{\partial}{\partial z_j} + \frac{1}{\rho_j}\frac{\partial}{\partial \rho_j}\frac{\rho_j}{m_j}\frac{\partial}{\partial \rho_j} + \frac{1}{\rho_j^2 m_j}\frac{\partial^2}{\partial \phi_j^2}\right)$$
$$\mp \frac{i}{2}\hbar\omega_{c,j}\frac{\partial}{\partial \phi_j} + \frac{1}{8}m_j\omega_{c,j}^2\rho_j^2 + V_j(z_j, \rho_j), \quad (3)$$

where $\omega_{c,j} = eB/m_j c$ are the electron and hole cyclotron frequencies and the vector potential is taken in the symmetrical gauge $\mathbf{A} = \frac{1}{2}B\rho\mathbf{e}_\phi$.

The one-particle wave functions are separable, $\Psi_j(z, \rho, \phi) = (1/\sqrt{2\pi})e^{il\phi}\xi_{j,i}^l(z_j, \rho_j)$, where $l = 0, \pm 1, \pm 2, \ldots$ is the angular momentum, and the wave functions $\xi_{j,i}^l(z_j, \rho_j)$ are eigenfunctions of the Hamiltonian

$$H_j^l = -\frac{\hbar^2}{2}\left(\frac{\partial}{\partial z_j}\frac{1}{m_j}\frac{\partial}{\partial z_j} + \frac{1}{\rho_j}\frac{\partial}{\partial \rho_j}\frac{\rho_j}{m_j}\frac{\partial}{\partial \rho_j}\right) + \frac{\hbar^2 l^2}{2m_j\rho_j^2} \pm \frac{l}{2}\hbar\omega_{c,j}$$
$$+ \frac{1}{8}m_j\omega_{c,j}^2\rho_j^2 + V_j(z_j, \rho_j), \quad (4)$$

where the index i denotes the eigenenergies of H_j^l. As a consequence of the axial symmetry of our problem, there is no coupling between the wave functions with different values of the total angular momentum L. Therefore, we can construct the exciton wave function Ψ_L with fixed total momentum L as the linear combination

$$\Psi_L(\mathbf{r}_1, \mathbf{r}_2) = \sum_{l=-l_m}^{l_m} \psi^l(\chi)e^{i(l/2)(\phi_1 - \phi_2) + i(L/2)(\phi_1 + \phi_2)}, \quad (5)$$

where the functions $\psi^l(\chi)$ obey the Schrödinger equation

$$\sum_{j=1}^{2} H_j^l \psi^l(\chi) + \sum_{l'=-l_m}^{l_m} V_C^{l-l'}(\chi)\psi^{l'}(\chi) = E\psi^l(\chi), \quad (6)$$

with E the eigenenergy, for brevity χ denotes the coordinates $(z_1, z_2, \rho_1, \rho_2)$, V_C^l is the matrix element of the Coulomb interaction

$$V_c^l(\chi) = -\frac{e^2}{\epsilon}\frac{1}{2\pi}$$
$$\times \sum \int_0^{2\pi} d\phi \frac{e^{-il\phi}}{\sqrt{(z_1-z_2)^2 + \rho_1^2 + \rho_2^2 - 2\rho_1\rho_2\cos(\phi)}}, \quad (7)$$

and $L_m = 2l_m + 1$ is the total number of angular harmonics in the expansion.

A common technique to solve the eigenvalue problem is to use an expansion of the wave function in a suitable set of basis functions. For the typical sizes of the quantum disks considered here, the exciton binding energy is much smaller than the confinement energy. As a consequence, a natural choice is to take the eigenfunctions $\xi_{j,i}^l$ of the one-particle Hamiltonian. But for our present problem such an approach runs into obstacles because of the enormous number of basis functions that are required to obtain the binding energy with sufficient accuracy. Indeed, using the one-particle eigenfunctions for different values of the angular momentum l and quantum number $i = 1, \ldots, I$, one has to calculate $L_m I^4$ matrix elements of the Hamiltonian. In the present case of hard wall confinement, the one dimensional eigenfunctions are too complicated in order to obtain an analytical expression for the Coulomb matrix elements. Therefore, a numerical integration procedure has to be used on the space grid with size $N_g = (K \times N)^2$, where K, N are the numbers of grid points for the longitudinal and transverse directions, respectively. In principle, the difficulties in the calculation of the Coulomb matrix elements can be avoided by applying an appropriate basis, for instance, the nonorthogonal Gaussian basis, which is widely employed in quantum-chemical simulations. But in this case there is an increase of the number of functions that are needed, leading to difficulties with diagonalizing a large $L_m I^2 \times L_m I^2$ nonsparse matrix. Note that for an arbitrary basis, the number $I = i_z i_r$ is determined by the number of one-particle wave functions in the longitudinal (i_z) and the radial (i_r) directions. The total number of operations depends crucially on the considered number of subbands i_z in the z direction. For a small ratio d/R of the longitudinal to transverse size of the quantum disk as given before, we can limit ourself by taking only one subband.[15,16]

A. 3D exciton problem

For arbitrary values of the ratio d/R we present a numerical technique based on the use of a finite difference scheme. Let z_k ($k = 1, \ldots, K$) and ρ_n ($n = 1, \ldots, N$) be some nonuniform space grid in the longitudinal and transverse directions for both electron and hole coordinates. Using the appropriate symmetry conditions for the ground-state wave function in the longitudinal direction $\partial\psi/\partial z_j(z_j = 0) = 0$ we can limit ourselves to the region $z_j > 0$. Thus, the first point of the z grid corresponds to $z = 0$. The upper ($z_K > d/2$) and right

$(\rho_N > R)$ boundaries of the simulation region correspond to the barrier region where the wave function and its derivatives go to zero. Therefore, the Neumann conditions $\partial \psi / \partial z_j = 0$, $\partial \psi / \partial \rho_j = 0$ are employed for these boundaries. To obtain the finite difference scheme for the one-particle Hamiltonian, including the discontinuous behavior of the particle mass and external potential, we integrate the expression over the square $(z_{k-1/2} < z < z_{k+1/2}, \ \rho_{n-1/2} < \rho < \rho_{n+1/2})$, where the subgrids with noninteger indexes are determined by the relations $z_{k+1/2} = (z_{k+1} + z_k)/2, \rho_{n+1/2} = (\rho_{n+1} + \rho_n)/2, z_{-1/2} = \rho_{-1/2} = 0$. Substituting the finite difference expressions for the derivatives of the wave function $\partial \psi / \partial z (z = z_{k+1/2}) = (\psi_{k+1} - \psi_k)/(z_{k+1} - z_k), \partial \psi / \partial \rho (\rho = \rho_{n+1/2}) = (\psi_{n+1} - \psi_n)/(\rho_{n+1} - \rho_n)$ we obtain the following finite difference scheme for the one-particle Hamiltonian:

$$(\hat{H}_j^l \psi)_{k,n} = -a_j^{k,n} \psi_{k+1,n} - c_j^{k,n} \psi_{k-1,n} - b_j^{k,n} \psi_{k,n+1}$$
$$- d_j^{k,n} \psi_{k,n-1} + p_j^{k,n} \psi_{k,n}, \qquad (8)$$

with the coefficients

$$a_j^{k\neq 1,n} = \hbar^2 (1/m_{jz}^{k,n} + 1/m_{jz}^{k-1,n})/2(z_k - z_{k-1})h_{z,k},$$
$$a_j^{k=1,n} = 0, \qquad (9a)$$

$$c_j^{k\neq K,n} = \hbar^2 (1/m_{jz}^{k,n} + 1/m_{jz}^{k+1,n})/2(z_{k+1} - z_k)h_{z,k},$$
$$c_j^{k=K,n} = 0, \qquad (9b)$$

$$b_j^{k,n\neq 1} = \rho_{n-1/2}\hbar^2 (1/m_{j\rho}^{k,n} + 1/m_{j\rho}^{k,n-1})/2(\rho_n - \rho_{n-1})h_{\rho,n},$$
$$b_j^{k,n=1} = 0, \qquad (9c)$$

$$d_j^{k,n\neq N} = \rho_{n+1/2}\hbar^2 (1/m_{j\rho}^{k,n} + 1/m_{j\rho}^{k,n+1})/2(\rho_{n+1} - \rho_n)h_{\rho,n},$$
$$d_j^{k,n=N} = 0, \qquad (9d)$$

$$p_j^{k,n} = a_j^{k,n} + b_j^{k,n} + c_j^{k,n} + d_j^{k,n} + \frac{\hbar^2 l^2}{2\rho_n^2 m_j^{k,n}} \pm \frac{l}{2}\hbar \omega_{c,j}^{k,n}$$
$$+ \frac{1}{8}m_j^{k,n}(\omega_{c,j}^{k,n})^2 \rho_n^2 + V_j^{k,n}, \qquad (9e)$$

where $h_{z,k} = z_{k+1/2} - z_{k-1/2}$, $h_{\rho,n} = (\rho_{n+1/2}^2 - \rho_{n-1/2}^2)/2$. Due to the discontinuity of the mass and the external potential at the disk boundary, special care must be taken in the choice of the expression for its grid values. In the expressions the averaged value of the masses $m_{jz}^{k,n}, m_{j\rho}^{k,n}, m_j^{k,n}$ and potential $V_j^{k,n}$ are determined by the following relations:

$$(m_{jz}^{k,n})^{-1} = h_{\rho,n}^{-1}\int_{\rho_{n-1/2}}^{\rho_{n+1/2}} \rho m_j^{-1}(z=z_k,\rho)d\rho,$$

$$(m_{j\rho}^{k,n})^{-1} = h_{z,n}^{-1}\int_{z_{n-1/2}}^{z_{n+1/2}} m_j^{-1}(z,\rho=\rho_n)dz,$$

$$(m_j^{k,n})^{-1} = h_{z,k}^{-1}h_{\rho,n}^{-1}\int_{z_{k-1/2}}^{z_{k+1/2}}dz\int_{\rho_{n-1/2}}^{\rho_{n+1/2}} \rho m_j^{-1}(z,\rho)d\rho,$$

$$V_j^{k,n} = h_{z,k}^{-1}h_{\rho,n}^{-1}\int_{z_{k-1/2}}^{z_{k+1/2}}dz\int_{\rho_{n-1/2}}^{\rho_{n+1/2}} V_j(z,\rho)\rho \ d\rho.$$

Once a finite difference Hamiltonian $\hat{H} = \delta_{l,l'}\Sigma_{j=1}^2 \hat{H}_j^l + V_c^{l,l'}\delta_{M,M'}$ has been constructed, we have to develop a technique to obtain the ground state of the sparse matrix $\hat{H}$. Here $\delta_{i,j}$ is the unit matrix, index M denotes all indexes corresponding to the space grid. Note that the number of nonzero elements of the matrix $\hat{H}$ is only proportional to $L_m^2 N_g$. This is a key distinction from the commonly accepted expansion over basis functions, where this number increases as the second power with the number of functions. However, the size of our matrix is still large and therefore direct diagonalization methods are not suitable for solving our problem. The best approach to find only the lowest eigenvalue E_g and eigenvector Ψ is the inverse iteration method, where the eigenvector Ψ^i at the ith stage of the iteration is obtained by solving the following equation:

$$(\hat{H} - \lambda \delta_{l,l'}\delta_{M,M'})\bar{\Psi}^i = \Psi^{i-1}, \qquad (10)$$

with the subsequent normalization

$$\Psi^i = \bar{\Psi}^i / \sqrt{\langle \bar{\Psi}^i, \bar{\Psi}^i \rangle}, \qquad (11)$$

where the brackets $\langle , \rangle$ stand for scalar multiplication. The eigenenergy is obtained in the usual way $E_g^i = \langle \Psi^i, \hat{H}\Psi^i \rangle$. The value of the parameter $\lambda < E_g$ is chosen such that a minimum absolute value of the matrix $(\hat{H} - \lambda \delta_{l,l'}\delta_{M,M'})$ corresponds to the ground state of the matrix $\hat{H}$. There exist many numerical relaxation techniques to solve the boundary value problem. Using standard methods one has to solve the equation with good precision at each stage of the inverse iteration procedure. Here, we propose a technique that generalizes in fact the commonly accepted Gauss-Seidel methods[17] with inverse iterations. The value of the eigenvector Ψ^i for the mesh points $(l,m = k_1, n_1, k_2, n_2)$ is obtained by using the following relation:

$$\Psi_i = (\Psi_{i-1} + \alpha_{i-1}\Theta_1 + \Theta_2) \left/ \left(\sum_{j=1}^2 p_j + V_c^{ll} - \lambda\right), \right. \qquad (12)$$

where

$$\Theta_1 = \sum_{j=1}^2 (c_j\Psi_{i-1}^{k_j+1} + d_j\Psi_{i-1}^{n_j+1}) - \sum_{l'>l}^{l_m} V_c^{l,l'}\Psi_{i-1}^{l'}, \qquad (13a)$$

$$\Theta_2 = \sum_{j=1}^2 (a_j\Psi_i^{k_j-1} + b_j\Psi_i^{n_j-1}) - \sum_{l=l_m}^{l<l'} V_c^{l,l'}\Psi_i^{l'}. \qquad (13b)$$

For the ground state $\bar{\Psi}_i = \Psi_{i-1}/(E_g - \lambda)$, we found that the maximum rate of convergency is realized by using the following values of the parameters: $\alpha_{i\neq 1} = 1/(E_g^i - \lambda)$ and $\alpha_{i=1} = 1$.

B. 2D exciton problem

For quantum disks with large radius $R \gg d$ we use the adiabatic approach, a technique that was already successfully applied in Refs. 15 and 18. Within this approach, we can write the wave function as

$$\psi_l(\boldsymbol{\chi}) = \psi_1(z_1)\psi_2(z_2)\psi_l(\boldsymbol{\rho}_1,\boldsymbol{\rho}_2), \qquad (14)$$

where $\psi_j(z_j)$ corresponds to the ground state of the longitudinal Hamiltonian

$$H_{z,j} = -\frac{\hbar^2}{2}\frac{\partial}{\partial z_j}\frac{1}{m_j}\frac{\partial}{\partial z_j} + V_{j,z}(z_j), \qquad (15)$$

for electrons ($j=1$) and holes ($j=2$), respectively. Since the wave function penetrates only slightly into the barrier region in the radial direction, the longitudinal behavior of the effective masses m_j and the confinement potentials $V_{j,z}$ can, to high accuracy, be approximated by $m_{j,z} = m_j(z,\rho_j=0)$, $V_{j,z} = V_j(z,\rho_j=0)$. Then the wave function of the ground state has a simple form inside the disk, $\psi_j(|z|<d/2) = \cos(k_j z)$, and outside the disk, $\psi_j(|z|>d/2) = \exp(-\kappa_j|z|)$, where $k_j = \sqrt{2m_{w,j}E_{0,zj}}/\hbar$ and $\kappa_j = \sqrt{2m_{b,j}(V_{o,j}-E_{0,zj})}/\hbar$. The energy of the ground state $E_{0,zj}$ is obtained from the continuity of the wave function and conservation of the current $m^{-1}\partial\psi/\partial z$ at the boundary ($|z|=d$). Substituting expression (14) into the Schrödinger equation and integrating out the z_j coordinates by taking the average $\langle\psi_1(z_1)\psi_2(z_2)|H|\psi_1(z_1)\psi_2(z_2)\rangle = H^{2D}$, we obtain the effective two-dimensional Hamiltonian

$$H^{2D} = \sum_{j=1}^{2}\left[\left(\mathbf{p}_j - \frac{q_j}{c}\mathbf{A}_j\right)\frac{1}{2m_j'(\boldsymbol{\rho}_j)}\left(\mathbf{p}_j - \frac{q_j}{c}\mathbf{A}_j\right) + V_j'(\boldsymbol{\rho}_j)\right]$$
$$+ V_c'(\boldsymbol{\rho}_1 - \boldsymbol{\rho}_2), \qquad (16)$$

where $\mathbf{p}_j = -i\hbar\,\partial/\partial\boldsymbol{\rho}_j$, $V_j'(\rho_j) = V_j(z_j=0,\rho_j) - E_{0,zj}$, $m_j'(\rho_j > R) = m_{b,j}$,

$$\frac{1}{m'(\rho_j < R)} = \frac{1}{m_{w,j}}\int_0^{d/2}dz_j|\psi_j(z_j)|^2 + \frac{1}{m_{b,j}}\int_{d/2}^{\infty}dz_j|\psi_j(z_j)|^2, \qquad (17)$$

and the effective Coulomb interaction is

$$V_c'(\boldsymbol{\rho}) = -\frac{e^2}{\epsilon}\int_{-\infty}^{\infty}dz_1 dz_2\frac{|\psi_1(z_1)|^2|\psi_2(z_2)|^2}{\sqrt{(z_1-z_2)^2+|\boldsymbol{\rho}|^2}}. \qquad (18)$$

Using a Gaussian shape for the longitudinal wave function of the ground state, the authors of Ref. 19 have obtained an analytical approximation to the effective Coulomb potential

$$V_c'(\rho) = -\frac{e^2}{\epsilon}\frac{1}{\sqrt{2\pi}\gamma}e^{\rho^2/4\gamma^2}K_0\left(\frac{\rho^2}{4\gamma^2}\right), \qquad (19)$$

where K_0 is the modified Bessel function. For a system with infinite barriers the value $\gamma = 0.277d$ gives the best fit to the effective Coulomb potential. As a consequence of the penetration of the electron and hole into the barrier region, the value of γ/d increases with decreasing disk thickness. We
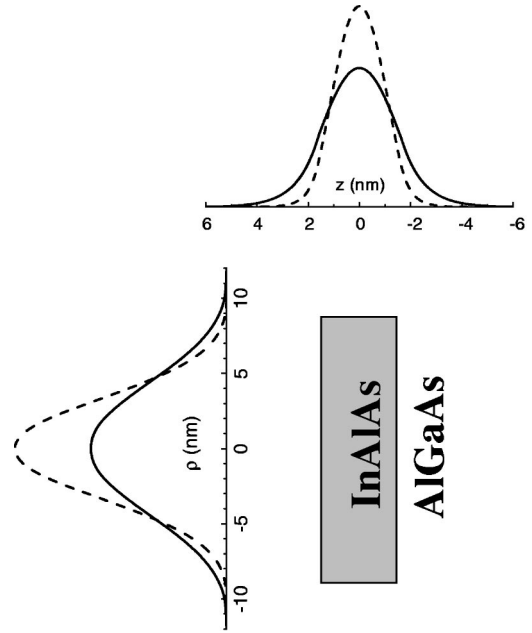

FIG. 1. Side view of the quantum disk together with the electron (solid curves) and hole (dashed curves) probability distribution along the ($\rho,z=0$) and the ($\rho=0,z$) direction.

have found that for our parameters of the quantum disk, $R = 8.95$ nm and $d=3.22$ nm, the value $\gamma=1.675$ nm gave the best fit to the results obtained from direct numerical calculation of the effective two-dimensional Coulomb potential. The other parameters of the two-dimensional Hamiltonian are $E_{0,ze}=116.06$ meV, $E_{0,zh}=38.13$ meV, $V_{oe}'=141.94$ meV, $V_{oh}'=133.87$ meV, $m_{we}'=0.080m_0$, $m_{be}'=0.097m_0$, $m_{wh}'=m_{bh}'=0.45m_0$, where indices e and h correspond to electron and hole, respectively. The numerical diagonalization technique for the 2D Hamiltonian was presented already in Ref. 15.

III. RESULTS AND DISCUSSION FOR THE EXCITON GROUND STATE

We have calculated the exciton ground-state energy and exciton binding energy as a function of an applied magnetic field. We used for our simulations the physical parameters of the $In_{0.55}Al_{0.45}As$ self-assembled quantum dots, used in the experiment by Wang et al.[11] The studied disks have a height of 3.22 nm and a radius of 8.95 nm. The other parameters were already given above. Figure 1 shows the probability distribution of the electron (solid curves) and hole (dashed curves) $|\psi_i(\mathbf{r}_i)|^2$, $i=e,h$, for the ground state along ($z=0,\rho$) and perpendicular ($z,\rho=0$) to the disk under consideration. Along the ρ direction, the electron and hole are confined within the disk, but along the z direction, there is appreciable penetration into the barrier material.

In Fig. 2 the exciton ground-state energy is plotted as a function of the magnetic field. This ground-state energy is given by

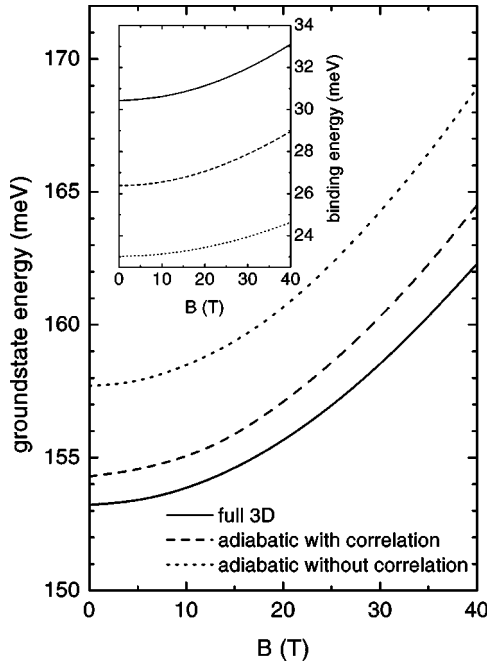$$E_0 = E^e + E^h + E_{\text{exc}}, \qquad (20)$$

FIG. 2. The exciton ground-state energy as a function of the magnetic field. The solid curve shows the result obtained within the full 3D treatment, whereas the dashed and dotted curves are the result for the adiabatic approximation, respectively, with and without correlation. In the inset, the exciton binding energy is plotted. The same curve conventions are used as in the main figure.

where E^e and E^h are the single electron and hole energies, respectively, and E_{exc} is the exciton binding energy. The solid curve shows the result of the full 3D treatment of the problem, whereas the dashed and dotted curves are calculated using the adiabatic approximation. For the latter case, we make a distinction between the cases with and without correlation. For the case without correlation, the Coulomb interaction is calculated using the single-particle electron and hole wave functions:

$$E_{exc} = -\frac{e^2}{\epsilon} \left\langle \psi^e \psi^h \left| \frac{1}{|\mathbf{r}_e - \mathbf{r}_h|} \right| \psi^e \psi^h \right\rangle. \quad (21)$$

The total exciton wave function was used in order to calculate the energy with correlation

$$E_{exc} = -\frac{e^2}{\epsilon} \left\langle \psi^{e,h} \left| \frac{1}{|\mathbf{r}_e - \mathbf{r}_h|} \right| \psi^{e,h} \right\rangle. \quad (22)$$

Figure 2 shows an enhancement of the ground-state energy with increasing magnetic field for all three cases. The correlation energy, which is given by the difference between the dotted and dashed curve, is 3.4 meV for $B=0$ T and increases to 4.4 meV for $B=40$ T.

The inset shows the exciton binding energy as a function of the magnetic field. Again we see an increase for increasing magnetic field as expected. This is not surprising, because by applying higher magnetic fields the particles are more confined, they are closer to each other and therefore more tightly bound, which implies an increase of the binding energy. The assignment of the different curves is the same as
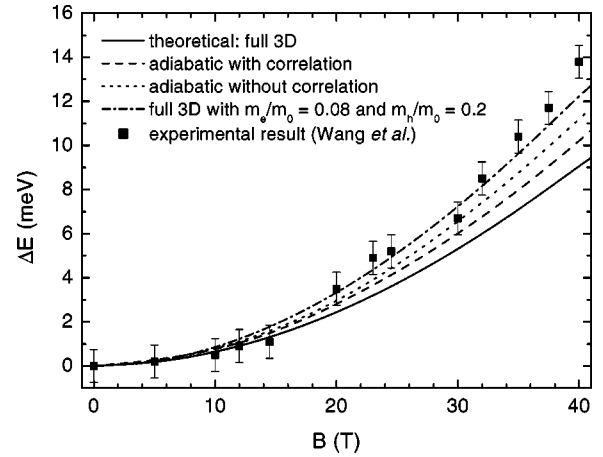

FIG. 3. The diamagnetic shift of the exciton energy as a function of an external magnetic field. The curves are our theoretical results within different approximations and the squares are the experimental results of Wang *et al.* (Ref. 11).

that for the ground-state energy (see main figure). Note that the inclusion of correlation increases the binding energy at $B=0$ T with 14.5% while the full 3D treatment of the problem further increases the binding energy with 13.6%.

From our calculation of the exciton ground-state energy, we can easily determine the diamagnetic shift of the exciton, which is defined by $\Delta E = E(B) - E(B=0)$. The result is shown in Fig. 3, where the curves indicate our calculated results for the three cases, as mentioned above, and the squares are the experimental results, as obtained by Wang *et al.*[11] From the comparison between the different approaches and experiment, we notice (1) for $B < 8$ T all three approaches give practically the same result, which agrees perfectly with experiment, (2) when B is increased above 8 T the three theoretical approaches have the same qualitative B dependence, but there are small quantitative differences in the slope of the curves, and (3) in the high-field regime, i.e., $B > 20$ T, our theoretical results substantially underestimate the experimental result. The masses used for these calculations were the ones given by Wang *et al.* in Ref. 11 ($m_{w,e} = 0.076m_0$, $m_{b,e} = 0.097m_0$, $m_h = 0.45m_0$), and it is clear that here the heavy-hole mass was used. However, in Ref. 20 it was argued that for a magnetic field normal to the sample plane, the light-hole mass should be used. Because the dot height is much smaller than the dot radius, heavy-hole character is expected in the growth direction for the ground hole state and light-hole character for in-plane motion. Including the effects of strain, they find for InAs dots that $m_e = 0.055m_0$ and $m_h = 0.1m_0$. Combining this with values for AlAs,[21] we find by linear interpolation to the material $In_{0.55}Al_{0.45}As$ values of $0.080m_0$ and $0.2m_0$ for, respectively, the electron and the hole mass. The result for the diamagnetic shift in this case is depicted as the dot-dashed curve in Fig. 3. This result is in very good agreement with the experimental results.

In previous theoretical work, only the exciton energy and wave function at $B=0$ were considered, from which the diamagnetic shift can be calculated as $\Delta E = \beta B^2$, where $\beta = e^2 \langle \rho^2 \rangle / 8\mu$ and $\langle \rho^2 \rangle$ is the mean quadratic electron-hole

distance. This is a good approximation in the case of low magnetic fields, when the magnetic confinement is much lower than the confinement due to the quantum dot. However, for higher magnetic fields, the magnetic confinement becomes more important. Then the quadratic dependence of the energy shift on the magnetic field will change into a linear dependence, due to the formation of Landau levels. In this case the energy shift becomes $\Delta E = \hbar(\omega_{c,e} + \omega_{c,h})$, where $\omega_{c,i} = eB/m_i$ is the cyclotron frequency. With this knowledge, one can construct the function

$$\Delta E = \frac{\beta B^2}{1 + \alpha B}, \tag{23}$$

which interpolates between the small and large magnetic-field behavior and where β and α are taken as fitting parameters. This formula gives for low magnetic fields ($B \rightarrow 0$) the already known expression $\Delta E = \beta B^2$, and for high magnetic fields ($B \rightarrow \infty$) $\Delta E = (\beta/\alpha)B$. It turns out that Eq. (23) gives an extremely good fit to the numerical results of Fig. 3 for $\beta = 6.37$ μeV T^{-2} and $\alpha = 3.06 \times 10^{-3}$ T^{-1}. We found that the fitted curve reproduces the solid curve in Fig. 3 so well that they cannot be discriminated. We also calculated β using the expression $\beta = e^2\langle\rho^2\rangle/8\mu$ for $B \rightarrow 0$, which resulted into the value $\beta = 8.89$ μeV T^{-2}. This value is substantially higher than the one found by fitting. In the other limit, we compare $\Delta E = (\beta/\alpha)B$ with $\Delta E = \hbar\omega_c = (\hbar e/\mu)B$, where $\mu = m_e m_h/(m_e + m_h)$ is the effective exciton mass in In$_y$Al$_{1-y}$As. Such a calculation gives $\hbar e/\mu = 1.69 \times 10^{-3}$ eV T^{-1}, which is smaller than the fitted value $\beta/\alpha = 2.08 \times 10^{-3}$ eV T^{-1}. The fitted results within the adiabatic approximation with and without correlation are respectively, $\beta = 7.56$ μeV T^{-2}, $\beta/\alpha = 1.52 \times 10^{-3}$ eV T^{-1} and $\beta = 7.79$ μeV T^{-2}, $\beta/\alpha = 2.75 \times 10^{-3}$ eV T^{-1}. Using the light-hole mass instead of the heavy-hole mass, we find, respectively, the following fitted and calculated results: $\beta = 8.84$ μeV T^{-2}, $\beta/\alpha = 2.351$ meV T^{-1} and $\beta = 14.08$ μeV T^{-2}, $\beta/\alpha = 1.96$ meV T^{-1}.

In the above calculations we investigated the adiabatic shift, which is a relative quantity, and therefore in the calculation of the ground-state energy, the band gap was not included. But when we want to compare the experimental excitation energy, the band gap of the disk material is needed. For $B = 0$ T, using the heavy-hole mass, we found a ground-state energy of $E = E^e + E^h + E_{exc} = 152.2$ meV, using Eq. (20). For the case of the light-hole mass, which gave a better agreement with the experimental results, the ground-state energy at $B = 0$ T is 178.5 meV. To obtain the total excitation energy, as measured in photoluminescence experiments, e.g., by Wang et al.,[11] the band-gap energy E_g has to be added to this equation:

$$E = E^e + E^h + E_{exc} + E_g. \tag{24}$$

For our study, we considered In$_{0.55}$Al$_{0.45}$As/Al$_{0.35}$Ga$_{0.65}$As quantum dots. Without strain, the band-gap energy of the dot material was obtained by linear interpolation between the result for InAs ($E_g = 0.41$ eV) and AlAs ($E_g = 3.13$ eV), which results in $E_g = 1.634$ eV, whereas we found for the barrier material that $E_g = 2.083$ eV.[22,23] The difference in
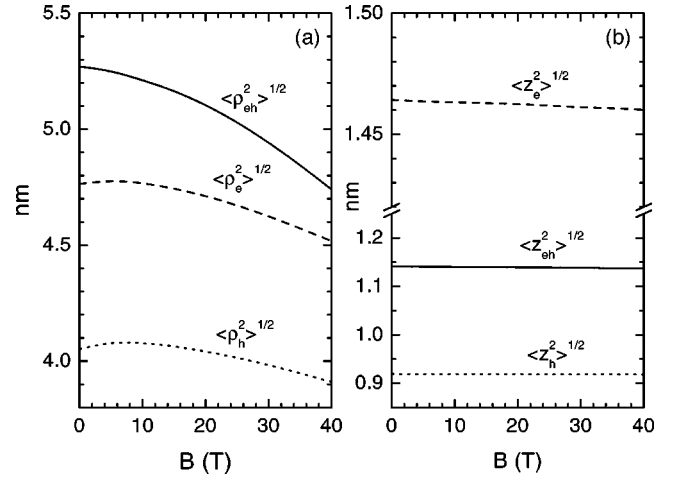
FIG. 4. The extent of the electron, the hole, and the exciton as a function of the magnetic field, along the radial (a) and longitudinal (b) direction, respectively.

band-gap energy between the two materials is $\Delta E_g = 450$ meV. For the total exciton energy, we now find $E = 1.634$ eV$+0.1532$eV$(0.1793$eV$) = 1.787$ eV$(1.8133$ eV$)$ using respectively the heavy- (light-) hole mass. From Ref. 11, we know that the band-gap difference between the dot and the barrier material, corrected for strain effects, is $\Delta E_g = 430$ meV. This means that the band gap of the dot material has increased by 20 meV. For the total exciton energy, this gives us the final result of $E = 1.81$ eV using the heavy-hole mass and $E = 1.83$ eV using the light-hole mass. In the experiments, for $B = 0$ T, the value of $E = 1.894$ eV was found, which gives reasonable agreement with our theoretical result in view of the fact that the composition of the alloy in the dot can, for example, not be uniform, the dot size is not known with high accuracy, etc.

Next, we investigated the effect of an applied magnetic field on the exciton characteristics, using the parameters corresponding to the solid curve in Fig. 3. First we considered the one-particle characteristics $\langle z_e^2 \rangle^{1/2}$, $\langle z_h^2 \rangle^{1/2}$, $\langle \rho_e^2 \rangle^{1/2}$, and $\langle \rho_h^2 \rangle^{1/2}$, where z_e, z_h and ρ_e, ρ_h are the electron and hole coordinates along the z axis and in the plane, respectively. The results are shown in Fig. 4 and were calculated using the full 3D approach. The figure shows clearly the squeezing of the exciton due to the magnetic field, especially for the in-plane direction. The mean quadratic electron-hole separations $\langle \rho_{eh}^2 \rangle^{1/2}$ and $\langle z_{eh}^2 \rangle^{1/2}$ give an idea of the size of the exciton. We defined $\rho_{eh} = |\boldsymbol{\rho}_e - \boldsymbol{\rho}_h|$ and $z_{eh} = |z_e - z_h|$. Notice that the size of the exciton is comparable to the disk size. We see a more substantial decrease with increasing magnetic field than for the single-particle wave function, which agrees with the increased binding of the exciton.

In Fig. 5 the percentage of the electron (right scale in Fig. 5) and hole (left scale in Fig. 5) wave function in the dot is shown with varying magnetic field. Both the results for the 2D case with correlation and the full 3D treatment were calculated. More than 90% of the hole is inside the dot while only 71$-$73 % of the electron is inside the dot. With increasing magnetic field both the electron and hole become more confined inside the dot, indicating further squeezing due to
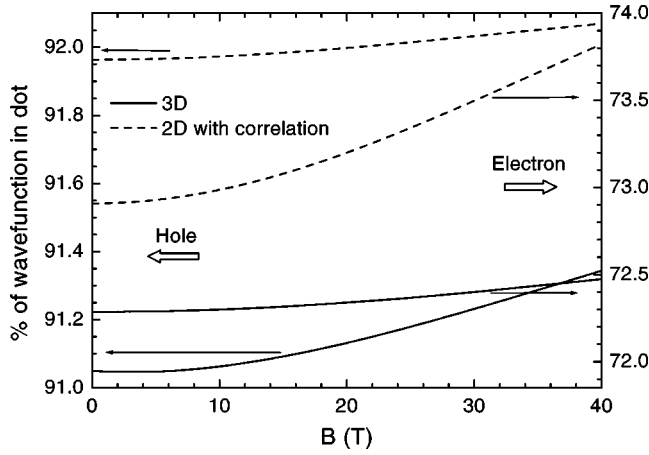
FIG. 5. The percentage of the wave function in the dot as a function of the magnetic field, both for the electron (right axis) and the hole (left axis). The solid curves are the result for the 2D case with correlation; the dashed curves are the result obtained within the full 3D treatment.

the magnetic field. For the hole, we observe a flattening of the curve at very high magnetic fields, both for the 3D calculation and for the 2D case. For high magnetic fields, the hole wave function is in the ρ direction totally confined in the dot. However, there is still some extent of the wave function outside the dot in the z direction. But since the magnetic field has almost no influence on the z direction, applying higher magnetic fields will not cause a further increase of the amount of the wave function inside the dot, and there will always be a small part of the wave function outside the dot.

Figures 6(a) and 6(b) are contour plots of the density distribution, of the electron and hole, respectively, along a cross section in the middle of the quantum dot perpendicular to the y direction. The electron density is defined as

$$|\psi_e(\boldsymbol{\rho}_e, z_e)|^2 = \int dz_h \int d\boldsymbol{\rho}_h |\psi^{e,h}(\boldsymbol{\rho}_e, z_e, \boldsymbol{\rho}_h, z_h)|^2 \quad (25)$$

and similarly for the hole. The solid curves show the result for the case of $B = 0$ T, whereas the dashed curves are the result for $B = 40$ T. The dashed square indicates the position of the disk, which is only one-fourth of the actual disk size. Due to the magnetic field, we see an increase in the density inside the dot, both for electrons and holes. Along the ρ direction the particles become more centered in the middle of the dot due to the squeezing by the applied magnetic field. However in the z direction, it seems at first sight that there is an expansion instead of the expected squeezing, but a closer look (by normalizing the function to its central value) tells us that this is not the case. Of course, the magnetic field is applied along the z axis and has no direct influence on the exciton behavior in the z direction. In the ρ direction, however, the magnetic field brings the electron and hole closer together. This implies a stronger interaction and we expect that this effect should also be seen in the z direction. This is also the case for the mean quadratic hole $\langle z_h^2 \rangle^{1/2}$ and electron-hole separation $\langle z_{eh}^2 \rangle^{1/2}$ (see Fig. 4), which decrease as a function of the magnetic field.
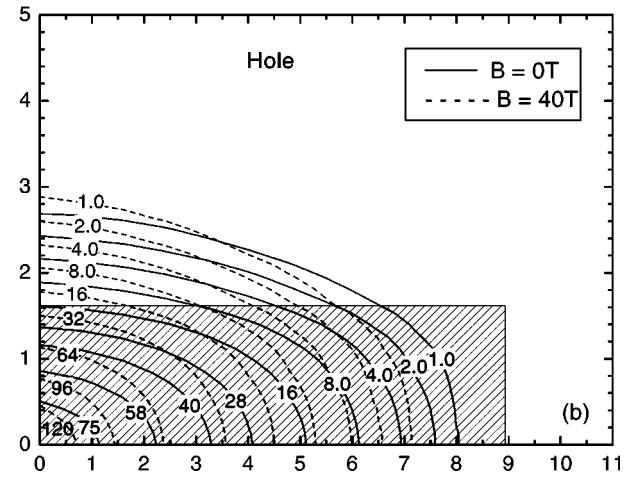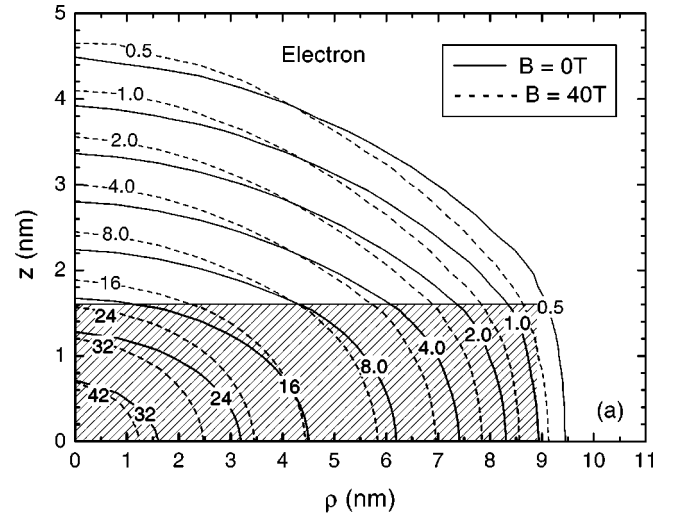

FIG. 6. Contour plot of the (a) electron and (b) hole density in a plane through the center of the quantum dot with size $R = 8.95$ nm and $d = 3.22$ nm. The plot shows only one quarter of the total space. Results are shown for $B = 0$ T (solid curves) and for $B = 40$ T (dashed curves).

IV. EFFECT OF CHANGING THE DISK RADIUS

We investigated the effect of the size of the disk on the exciton binding energy, which is depicted in Fig. 7 for the case with the full 3D treatment, for the parameters corresponding to the solid curve in Fig. 3. When varying the disk radius from $R = 1$ nm up to $R = 15$ nm (the dot thickness was fixed to $d = 3.22$ nm), we see initially a strong increase of the exciton energy by more than a factor of 2 and beyond $R \simeq 2.5$ nm it decreases slowly for increasing R. In the "large" R region, the binding energy increases for decreasing disk radius due to the larger confinement of the electron and hole wave function. The electron and hole are forced to sit closer to each other, which leads to an enhancement of the binding energy. This behavior continues until the disk radius reaches a value of $R \simeq 2.5$ nm, where the binding energy reaches a maximum value of $E_{exc} = 47$ meV. The decrease in the binding energy with decreasing R is due to the fact that the wave function of the particles start to spill over into the barrier material, i.e., the electron and the hole become less confined,
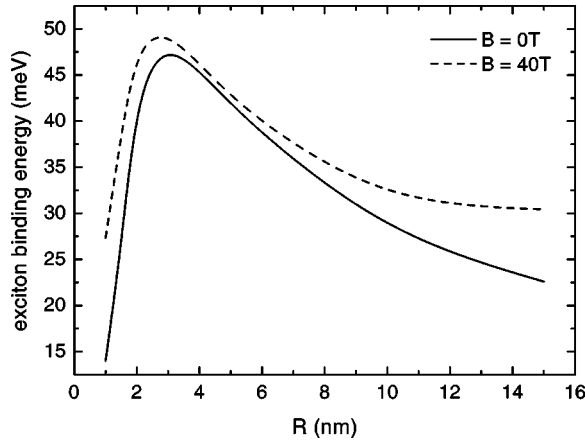
FIG. 7. The exciton binding energy as a function of the disk radius R for a disk thickness of $d = 3.22$ nm. Results are shown for two magnetic fields as indicated.

FIG. 9. Electron-hole separation in the z direction as a function of R. The inset shows the radial electron-hole separation as a function of R.

which leads to a much smaller interaction and therefore a lower binding energy. This is due to the competition between the confinement kinetic energy and the barrier material potential energy. This is confirmed by Fig. 8, where the percentage of the electron and hole wave function inside the dot is shown as function of the disk radius. For $R > 6$ nm these percentages increase very slowly with increasing R. We never reach 100% because of the substantial penetration of the wave function in the barrier material along the z direction (the thickness of the dot is only $d = 3.22$ nm). Note that for $R = 1$ nm less than 2% of the electron wave function but 24% of the hole wave function is inside the dot.

The effect of a magnetic field on the dot size dependence of the exciton energy is also shown in Fig. 7 for the case of $B = 40$ T. Notice that the largest B dependence is found for very small and very large R. In both situations the confinement of the electron and hole is smallest, and consequently the ratio between the magnetic energy and the confinement energy is largest. For intermediate dot size, i.e., 3 nm$< R$ < 7 nm we observe the smallest effect of a magnetic field on

the exciton energy. This is the region of dot size where the confinement potential is able to strongly confine the electron and hole to a small region in space.

We also investigated the effect of varying R on the electron-hole separation, both in the ρ and in the z direction. Figure 9 shows the result for $\langle z_{eh}^2 \rangle^{1/2}$, and we see a rather high starting value at $R = 1$ nm, decreasing strongly for increasing R. This high value at small R follows from the fact that a large part of the wave function is outside the dot, so the particles are not really confined anymore, which means that they are farther away from each other. The inset of Fig. 9 shows the electron-hole separation in the ρ direction. Also here, we start with a high value at very small R, followed by a strong decrease and a minimum of $\sqrt{\langle \rho_{eh}^2 \rangle} = 3.12$ nm at $R \simeq 3$ nm. Further increasing R, we find again an enhancement of $\langle \rho_{eh}^2 \rangle^{1/2}$, which initially is linear in R, but for $R > 12$ nm starts to level off and reaches a constant value in the limit $R \rightarrow \infty$.

The low-magnetic-field diamagnetic coefficient $\beta = e^2 \langle \rho_{eh}^2 \rangle / (8\mu)$, can be obtained from the results of Figs. 8 and 9, where μ is the effective exciton mass. The result is shown in Fig. 10 and we see a similar behavior as for the
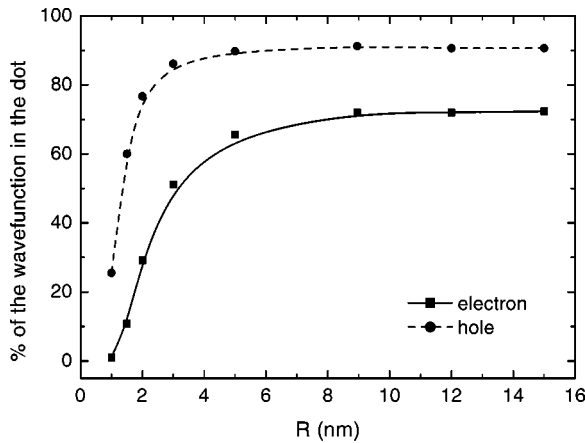

FIG. 8. The percentage of the electron (solid curve) and hole (dashed curve) wave function in the dot as a function of the disk radius R. Symbols are the calculated points and the curve is a guide to the eye.
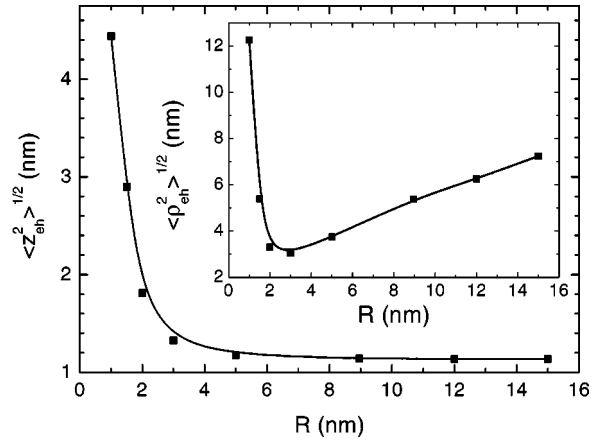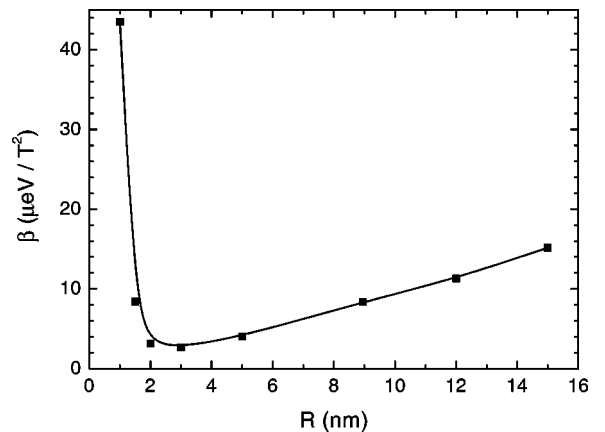

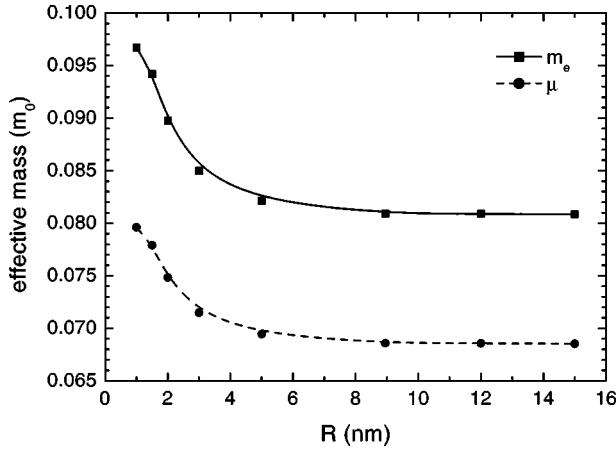FIG. 10. The diamagnetic coefficient β as a function of the disk radius R for $d = 3.22$ nm.

FIG. 11. The effective electron (solid curve) and exciton (dashed curve) masses as a function of the disk radius R.

FIG. 12. The exciton energy states for different values of the radial quantum number N, as a function of the magnetic field for $L=0$. Four different disk radii are considered: (a) $R=8.95$ nm, (b) $R=5$ nm, (c) $R=15$ nm, and (d) $R=30$ nm.

radial electron-hole separation (inset of Fig. 9). When calculating β, we took into account the variation of the effective exciton mass μ with varying disk radius. The effective mass is defined as

$$\frac{1}{\mu} = \frac{1}{m_e} + \frac{1}{m_h}, \qquad (26a)$$

with

$$\frac{1}{m_e} = \frac{1-P_w}{m_{e,b}} + \frac{P_w}{m_{e,w}}, \qquad (26b)$$

where $m_{e,b}=0.097m_0$ and $m_{e,w}=0.076m_0$ are the effective electron masses in, respectively, the barrier and the well and P_w is the probability to find the electron in the well. In Fig. 8 we showed that there is a considerable change of P_w for varying R, and this will have an effect on m_e and μ. For the hole we have the same mass in and outside the well, and therefore $m_h=0.45m_0$ is independent of R. In Fig. 11, the evolution of m_e and μ is depicted as a function of R. We see that for very small disks, where most of the wave function is outside the dot, the value of m_e converges to $m_{e,b}$ as expected. For larger disk radii, this value decreases and for $R \rightarrow \infty$ it reaches the limit $m_e=0.0809m_0$, which is larger than $m_{e,w}$ due to the penetration of the electron along the z direction in the barrier because of the small thickness of the disk.

V. EXCITON ENERGY SPECTRUM

The higher radial excited states ($N \neq 0$) for angular momentum $L=0$ are calculated within the adiabatic approximation. The result for a disk with radius $R=8.95$ nm and thickness $d=3.22$ nm is shown in Fig. 12(a), which clearly shows the appearance of an anticrossing of levels for higher-N states, and the energy scale for such states is also substantially larger than for the angular momentum states. This anticrossing is due to the fact that we consider a fixed angular momentum L for all states, which is a conserved quantity. The states with fixed L are nondegenerate. Again we considered cases of different disk radii and we observe an enhancement of the anticrossing for smaller disks [Fig. 12(b)] and a
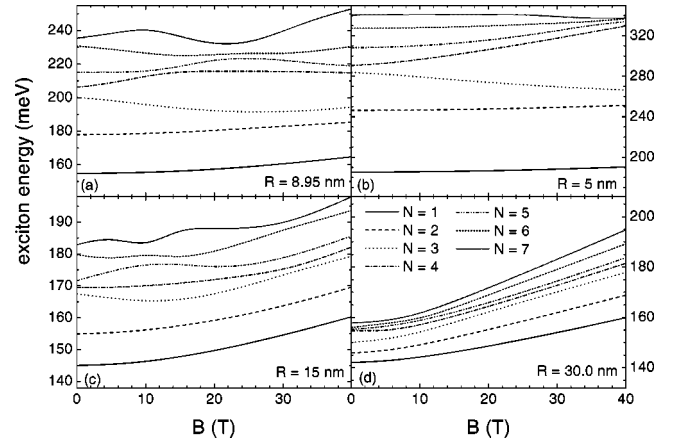
diminishing of the anticrossing for larger disks [Figs. 12(b) and 12(c)].

To study the anticrossing more closely, we considered the disk with $R=8.95$ nm and $d=3.22$ nm (parameters corresponding to the dashed/dotted curve in Fig. 3 were used). For the 2D problem, the radial part of the exciton wave function for a fixed L can be written as (see also Ref. 15)

$$\psi(\boldsymbol{\rho}_e, \boldsymbol{\rho}_h) = \sum_{k=1}^{k=k_n} \sum_{n=1}^{n=k_n} \sideset{}{'}\sum_{l=l_m}^{l=-l_m}$$
$$\times C_{kn}^l R_{k,(L+l)/2}(\rho_e) R_{n,(L-l)/2}(\rho_h)$$
$$\times e^{i(l/2)(\phi_1-\phi_2)+i(L/2)(\phi_1+\phi_2)}, \qquad (27)$$

where k and n correspond to the energy levels of the one-particle problem of electron and hole, respectively, and l is the relative angular momentum. The sum Σ' indicates that only even values of the relative angular momentum l are taken when L is even, and odd values otherwise. By studying the values of the coefficients C_{kn}^l, we could distinguish which one-particle states contribute most to the total exciton state. In Fig. 13(a), the symbols on the curves indicate the dominant term contributing to Eq. (27). The inset in Fig. 13(b) gives the (l,n) value corresponding to the different symbols. Notice that k remains 1, while n can have higher values, which implies that the hole excited states are mixed into the exciton wave function. The single-particle hole states have lower energy, due to its higher effective mass. Notice that when we connect each symbol by a line, we obtain intersecting levels. Such a spectrum would be obtained if (l,k,n) would be conserved quantities. Because of the electron-hole interaction the different (l,k,n) single particle states are mixed, which leads to the anticrossing of the levels. Because L is a conserved quantity, crossings between different N states are prohibited, and therefore, for a fixed N, the system is forced to go to a different (l,k,n) state.

The symbols in Fig. 13(a) indicate only the dominant term in Eq. (27), while the total summation considers typically
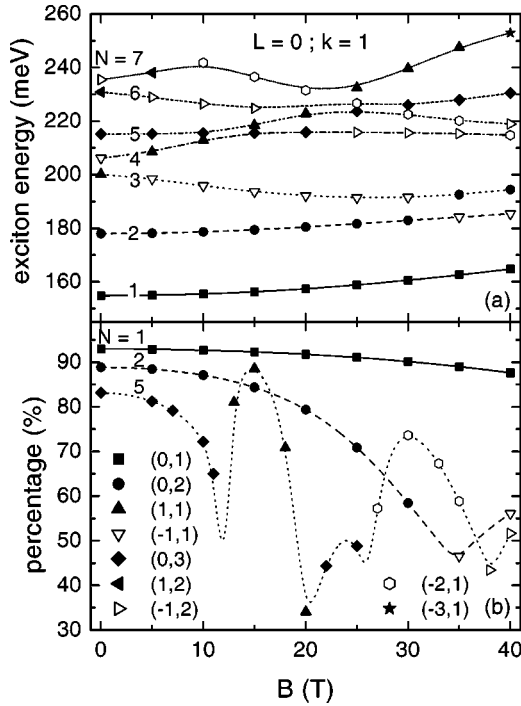
FIG. 13. (a) The higher excited radial states for $R=8.95$ nm and $d=3.22$ nm. The symbols indicate the (l,n) value of the most important single-particle state, where l is the relative angular momentum and n is the radial hole quantum number. (b) The percentage of the contribution of the most important state as a function of the magnetic field.

about 750 terms. In Fig. 13(b) we show how large the contribution of the dominant term is relative to the total sum of all terms. This percentage is defined as

$$\text{percentage} = \frac{|C_{kn}^l|^2}{\displaystyle\sum_{k,n,l} |C_{kn}^l|^2} \times 100. \qquad (28)$$

In Fig. 13(b) we only show the result for the case of $N=1,2,5$ in order not to overload the figure. We want to emphasize that, as a function of the magnetic field, the contribution of the dominant term, which can differ with increasing magnetic field, is shown and not the evolution of the contribution of a particular state. For $N=1$, the $(0,1,1)$ state appears to be very stable, as it stays between 85% and 95%. This means that there is very little mixing with other states. The $(0,1,2)$ state for $N=2$ is also very stable at low fields, but from $B=20$ T, the percentage drops, which indicates that another state is becoming important and serious mixing occurs. Finally at $B=35$ T the $(-1,1,1)$ state becomes most important, which can also be seen in Fig. 13(a). Now the percentage of the contribution of this $(-1,1,1)$ state is plotted and we see an increase with B. Also for $N=5$, the transitions between the successive states are clearly visible from Fig. 13(b). Each dip corresponds to a transition to another state with a consecutive anticrossing of the energy levels. A dip indicates strong mixing between two or even three states where the dominant state gives only a slightly higher contri-
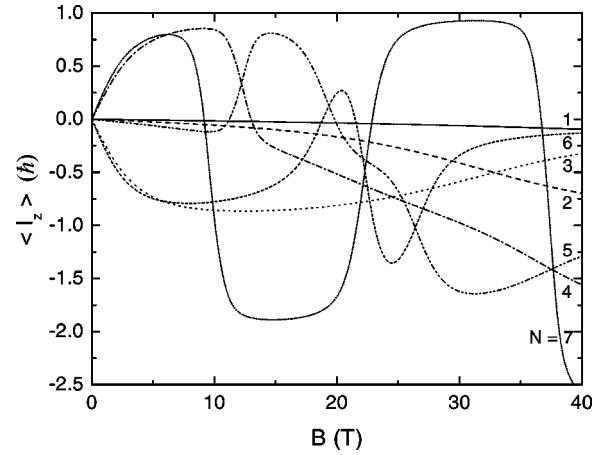

FIG. 14. The expectation value of the relative angular momentum operator l_z as a function of the magnetic field, for $L=0$ and different N states.

bution than the other important state(s). We see strong dips at $B=12$ T and $B=20$ T, which indicate the mixing between, respectively, $(0,1,3)\leftrightarrow(1,1,1)$ and $(1,1,1)\leftrightarrow(0,1,3)$. Comparison with Fig. 13(a) shows that these magnetic field values mark also the anticrossings between, respectively, $N=4\leftrightarrow N=5$ and $N=5\leftrightarrow N=6$. The height of the peaks is an indication of the stability of the state. At $B=15$ T, e.g., we see a very strong peak, whereas at $B=24$ T, only a small peak appears. Comparing with Fig. 13(a) we learn that, at the region between 20 and 30 T, there is a strong anticrossing and, although the system passes through the $(0,1,3)$ state, this state never becomes really important.

In the above discussion, we indicated the states with (l,k,n), where l is an integer number. However, the relative angular momentum l is not a good quantum number, because the operator l_z does not commute with the Hamiltonian and more specifically with the Coulomb interaction. Therefore the expectation value of the operator $l_z=(\hbar/i)\partial/\partial(\phi_1 -\phi_2)$ is expected not to be an integer. In Fig. 14 the expectation value $\langle l_z \rangle$ is depicted for the different N states as a function of the magnetic field, where $\langle l_z \rangle$ is calculated by

$$\langle l_z \rangle = \sum_{l,k,n} l |C_{kn}^l|^2. \qquad (29)$$

Notice that $\langle l_z \rangle$ tends to approach an integer value l when one of the terms in the sum of Eq. (27) dominates. The transition between states with different l is continuous. The more stable a state, the better it approaches an integer value l. The result for $N=7$, e.g., starts from $\langle l_z \rangle=0$ at $B=0$ T, then increases up to about $0.75\hbar$ and at $B=10$ T, drops down to $-1.8\hbar$ until $B=20$ T, where it starts to increase again, more slowly now, up to $\langle l_z \rangle=0.9\hbar$ for $B=25$ T, until finally at $B=40$ T it drops to less than $-2.5\hbar$. This agrees very well with the predicted integer values for l in Fig. 13(a). For other N states, the agreement might be less good, which is due to the stronger mixing with other states.

Finally, we considered the energy states for different values of the total angular momentum L within the adiabatic approximation. The result for a disk with radius $R=8.95$ nm
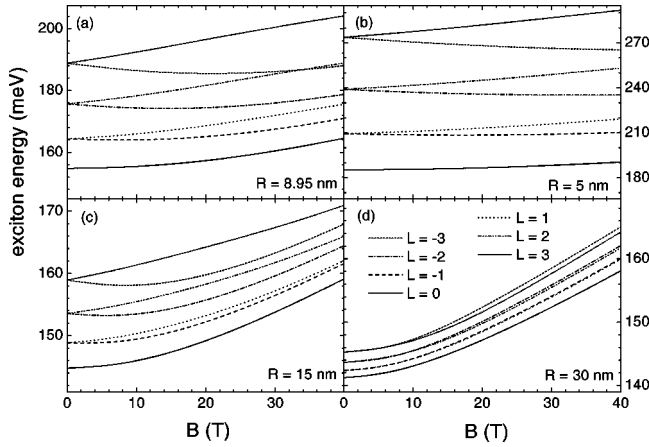
FIG. 15. The exciton energy states for different values of the total angular momentum L, as a function of the magnetic field. Four different disk radii are considered: (a) $R = 8.95$ nm (b) $R = 5$ nm, (c) $R = 15$ nm, and (d) $R = 30$ nm.

and thickness $d = 3.22$ nm is shown in Fig. 15(a) for the lowest radial state $N = 1$. Notice that for $B = 0$ T, the states with L and $-L$ are degenerate, which is lifted by a magnetic field. The corresponding splitting is the well-known Zeeman splitting. For a smaller disk radius, $R = 5$ nm, all energies are shifted to higher values, the splitting between the energy levels is larger, and the Zeeman splitting is increased [Fig. 15(b)]. When increasing disk radius R, i.e., $R = 15$ nm and $R = 30$ nm, the difference between the different angular momentum levels decreases and the energy shifts to lower values [Figs. 15(c) and 15(d)]. As in the previous case of different N states, here we also studied which single-particle (l,k,n) states are most important in the sum of Eq. (27) and the percentage of their contribution. Figure 16(a) denotes, for a disk with radius $R = 8.95$ nm and thickness $d = 3.22$ nm, the energies of the different L states, and the symbols indicate which (l,n) state is most important at a particular value of the magnetic field. Note that here both k and n remain 1. In Fig. 16(b) the percentage contribution of the particular (l,k,n) state is depicted. We see a transition occurring for the $L = -1, -2$ and -3 states. This follows also from Fig. 17, where the expectation value $\langle l_z \rangle$ of the relative angular momentum operator is plotted. For the $L = 0,1,2,3$ states, $\langle l_z \rangle$ remains quite constant, whereas for the other L states, $\langle l_z \rangle$ decreases towards a lower value of l. Because the total angular momentum is a conserved quantity, energy levels corresponding to different L values are allowed to cross; they do not mix.

VI. CONCLUSIONS

We calculated the ground-state energy (and the excited states), the binding energy, and the diamagnetic shift of an exciton in a quantum disk with radius R and thickness d for a hard wall confinement potential of finite height. The mass mismatch between the dot material and the surrounding material was taken into account. Our calculation is based on the finite difference technique, where we used three different theoretical approaches, which include the electron-hole cor-
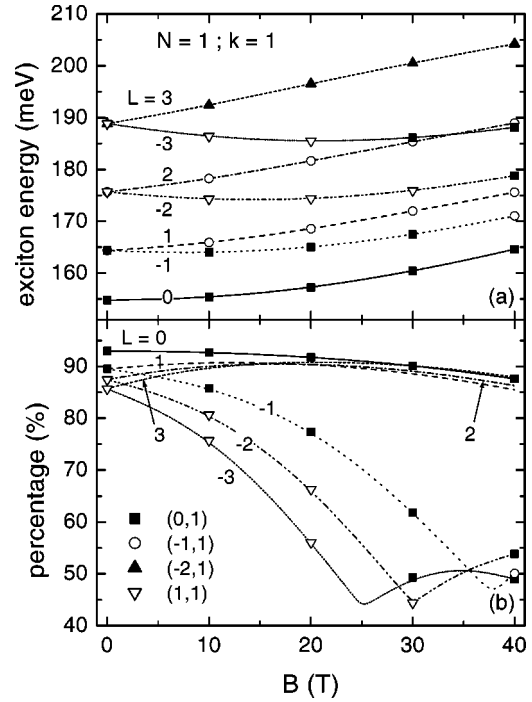

FIG. 16. (a) The energy states for different total angular momentum L for a disk with $R = 8.95$ nm and $d = 3.22$ nm. The symbols indicate the dominant single-particle (l,n) states and (b) gives the percentage of the contribution of this term to the total wave function.

relation on different levels. The 3D treatment is valid for arbitrary values of R and d and provides an "exact numerical" treatment of the exciton problem. For $R \gg d$, the adiabatic approach is applicable and here we distinguish the cases with and without correlation. The latter only uses the single-particle wave functions in order to calculate the exciton binding energy, whereas the first uses the total exciton wave function.

Under the influence of an external applied magnetic field up to 40 T, we find an increase of the exciton ground-state energy and binding energy. The electron-hole separation shows a squeezing of the exciton due to the magnetic field.
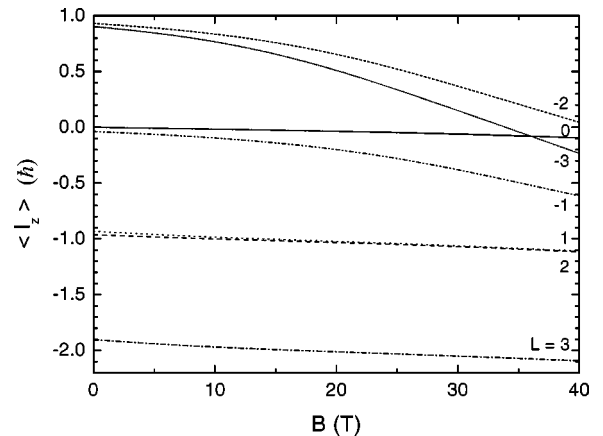

FIG. 17. The expectation value $\langle l_z \rangle$ for the different L states as a function of the magnetic fields.

This can also be seen from the electron and hole densities in and around the dot. Our theoretical results of the diamagnetic shift are in very good agreement with the experimental results of Ref. 11 if we assume that the light hole is involved in the exciton. This gives credibility to our modeling of self-assembled dots by a quantum disk, at least for the diamagnetic shift of the exciton energy.

When considering a varying disk radius R, we found a strongly decreasing exciton binding energy with decreasing R for very small R values, which indicates that the dots are too small to confine the exciton. This explanation is corroborated by an investigation of the radial electron-hole separation and of the percentage of the wave function in the dot, which indeed shows that, for very small R, a large part of the wave function is situated outside the dot. In the large R regime the exciton binding energy decreases with increasing R and approaches a constant value for $R \to \infty$. In the presence of an applied magnetic field, the exciton binding energy approaches a constant value for large disks much earlier than for the $B = 0$ T case, indicating that the dot confinement is dominated by the magnetic confinement.

Results for higher excited radial states, $N > 0$, show an anticrossing of levels that is more pronounced for small dot radius. The total angular momentum L is a conserved quantity. The relative angular momentum l, however, is not a good quantum number. Because of the coupling between the electron and the hole, the exciton wave function is a linear combination of all possible one-particle wave functions. We investigated which (l,k,n) states contribute most and how large its contribution is to the total exciton wave function. Furthermore we investigated the expectation value of the relative angular momentum operator l_z, which is not quantized and varies with the magnetic field. The degeneracy of the different total angular momentum states is lifted due to the presence of the confinement potential and the Zeeman splitting. This splitting decreases with increasing dot radius R. Also here we investigated the contribution of the one-particle states to the total exciton wave function. The energy states with different total angular momentum L can cross with varying magnetic field, because L is a good quantum number.

*Electronic mail: peeters@uia.ua.ac.be

†Permanent address: Institute of Theoretical and Applied Mechanics, Russian Academy of Sciences, Novosibirsk 630090, Russia.

[1] For a recent review see, e.g., D. Bimberg, M. Grundmann, and N.N. Ledentsov, in *Quantum Dot Heterostructures* (Wiley, Chichester, 1999).

[2] D. Bimberg, M. Grundmann, and N.N. Ledentsov, MRS Bull. **23**, 31 (1998).

[3] P.M. Petroff, Braz. J. Phys. **24**, 277 (1994).

[4] C. Pryor, Phys. Rev. Lett. **80**, 3579 (1998).

[5] G.W. Bryant, Phys. Rev. B **37**, 8763 (1988).

[6] J. Song and S.E. Ulloa, Phys. Rev. B **52**, 9015 (1995).

[7] V. Halonen, T. Chakraborty, and P. Pietiläinen, Phys. Rev. B **45**, 5980 (1992).

[8] P. Pereyra and S.E. Ulloa, Phys. Rev. B **61**, 2128 (2000).

[9] S. Le Goff and B. Stébé, Phys. Rev. B **47**, 1383 (1993).

[10] P.W. Fry, I.E. Itskevich, D.J. Mowbray, M.S. Skolnick, J.J. Finley, J.A. Barker, E.P. O'Reilly, L.R. Wilson, I.A. Larkin, P.A. Maksym, M. Hopkinson, M. Al-Khafaji, J.P.R. David, A.G. Cullis, G. Hill, and J.C. Clark, Phys. Rev. Lett. **84**, 733 (2000).

[11] P.D. Wang, J.L. Merz, S. Fafard, R. Leon, D. Leonard, G. Medeiros-Ribeiro, M. Oestreich, P.M. Petroff, K. Uchida, N. Miura, H. Akiyama, and H. Sakaki, Phys. Rev. B **53**, 16 458 (1996).

[12] M. Bayer, S.N. Walck, T.L. Reinecke, and A. Forchel, Phys. Rev. B **57**, 6584 (1998).

[13] A. Polimeni, S.T. Stoddart, M. Henini, L. Eaves, P.C. Main, K. Uchida, R.K. Hayden, and N. Miura, Physica E (Amsterdam) **2**, 662 (1998).

[14] S. Nomura, L. Samuelson, M.-E. Pistol, K. Uchida, N. Miura, T. Sugano, and Y. Aoyagi, Appl. Phys. Lett. **71**, 2316 (1997).

[15] F.M. Peeters and V.A. Schweigert, Phys. Rev. B **53**, 1468 (1996).

[16] G. Lamouche and Y. Lepine, Phys. Rev. B **51**, 1950 (1995).

[17] W.H. Press, B.P. Flannery, S.A. Teukolsky, and W.T. Vetterling, *Numerical Recipes* (Cambridge University Press, Cambridge, 1988), p. 674.

[18] J.M. Worlock, F.M. Peeters, H.M. Cox, and P.C. Morais, Phys. Rev. B **44**, 8923 (1991).

[19] R. Price, X. Zhu, S. Das Sarma, and P.M. Platzmann, Phys. Rev. B **51**, 2017 (1995).

[20] I.E. Itskevich, M. Henini, H.A. Carmona, L. Eaves, P.C. Main, D.K. Maude, and J.C. Portal, Appl. Phys. Lett. **70**, 505 (1997).

[21] M. Grundmann, O. Stier, and D. Bimberg, Phys. Rev. B **52**, 11 969 (1995).

[22] C. G. Van de Walle, Phys. Rev. B **39**, 1871 (1989).

[23] M. P. C. M. Krijn, Semicond. Sci. Technol. **6**, 27 (1991).